Coupled kinetic-fluid simulations on sputtering and transport of intrinsic carbon impurity in HL-3

Downloaded from: https://research.chalmers.se, 2026-08-31 18:23 UTC

Citation for the original published paper (version of record):

Liang, Z., Liu, Y., Feng, Y. et al (2026). Coupled kinetic-fluid simulations on sputtering and transport of intrinsic carbon impurity in
HL-3. Nuclear Materials and Energy, 48. http://dx.doi.org/10.1016/j.nme.2026.102206

N.B. When citing this work, cite the original published paper.

research.chalmers.se offers the possibility of retrieving research publications produced at Chalmers University of Technology. It covers all kind of research output: articles, dissertations, conference papers, reports etc. since 2004. research.chalmers.se is administrated and maintained by Chalmers Library

(article starts on next page)

Nuclear Materials and Energy 48 (2026) 102206

Contents lists available at ScienceDirect

Nuclear Materials and Energy

journal homepage: www.elsevier.com/locate/nme

Coupled kinetic-fluid simulations on sputtering and transport of intrinsic carbon impurity in HL-3

Z. Liang [a], Y.L. Liu [a], Y. Feng [a], S.Y. Dai [a,*], M. Hoelzl [b,c], A. Cathey [b], D. Hu [d], S.Q. Korving [e], Y.C. Liang [b], M. Szucs [b], Y. Zhang [f], D.Z. Wang [a,*], the JOREK Team [1]

[a] Key Laboratory of Materials Modification by Laser, Ion and Electron Beams (Ministry of Education), School of Physics, Dalian University of Technology, Dalian 116024, China
[b] Max Planck Institute for Plasma Physics, Boltzmannstr. 2, Garching b. M. 85748, Germany
[c] Chalmers University of Technology, Göteborg SE-41296, Sweden
[d] Beihang University, No. 37 Xueyuan Road, Haidian District, Beijing 100191, China
[e] ITER Organization, St. Paul Lez Durance Cedex 13067, France
[f] Southwestern Institute of Physics, Chengdu 610041, China

ARTICLE INFO

Keywords:
Carbon impurity sputtering
Coupled kinetic-fluid simulation
JOREK
HL-3

ABSTRACT

Carbon impurity sputtering and transport in the HL-3 tokamak are investigated using the time-dependent JOREK kinetic-fluid coupled framework with an updated sputtering model. Physical sputtering, chemical sputtering, and self-sputtering are treated simultaneously, with their yields evaluated dynamically from the evolving local plasma conditions. In the axisymmetric simulations, physical sputtering is localized near the strike point, whereas chemical sputtering extends over a broader target region. The sputtered carbon is subsequently transported along the divertor and scrape-off-layer flux tubes and exhibits a pronounced high-field-side/low-field-side asymmetry. During the simulated edge-localized-mode burst, the rapid increases in target temperature and deuterium ion flux strongly enhance and broaden physical sputtering, while chemical sputtering is suppressed near the strike point. Self-sputtering remains a secondary contribution under the conditions considered. These results demonstrate that the different sputtering channels respond differently to transient divertor conditions and should be treated self-consistently when modeling carbon source formation and transport in HL-3.

1. Introduction

Plasma-wall interaction (PWI) is a critical issue in magnetic confinement fusion devices because it affects both plasma performance and the lifetime of plasma facing components (PFCs) [1–3]. In the presence of edge localized modes (ELMs) [4], the sharply increased heat and particle fluxes onto PFCs can strongly enhance material sputtering and intrinsic impurity release [5]. In the divertor region, impurities can play a beneficial role by enhancing radiative power dissipation and mitigating target heat loads [6,7], whereas excessive impurity accumulation in the core plasma may lead to degradation of core energy confinement [8]. A detailed understanding of intrinsic impurity production and transport is therefore essential for assessing impurity effects on plasma behavior and optimizing divertor performance in present and future tokamaks.

Carbon-based plasma-facing components remain in use in present-day tokamaks [9–15], including HL-3. In these devices, sputtered carbon constitutes an intrinsic impurity source that can influence edge radiation, plasma-wall interaction, and divertor plasma conditions. A quantitative and self-consistent description of carbon sputtering and subsequent transport is therefore required to interpret experiments in devices with carbon-based plasma-facing components.

In this work, carbon impurity sputtering and its transport behavior in the HL-3 tokamak are investigated using the time-dependent JOREK [16–18] kinetic-fluid coupled framework [19,21]. The sputtering model is updated to simultaneously account for carbon impurities from physical sputtering, chemical sputtering, and self-sputtering. Note that the sputtering yields are dynamically evaluated during the simulation in response to the evolving local plasma parameters. The characteristics of physical and chemical sputtering are first examined under HL-3 plasma

* Corresponding authors.
E-mail addresses: daishuyu@dlut.edu.cn (S.Y. Dai), wangdez@dlut.edu.cn (D.Z. Wang).
[1] *See the author list of M. Hoelzl et al., Nucl. Fusion 61(6), 065001 (2021).*

https://doi.org/10.1016/j.nme.2026.102206
Received 22 June 2026; Received in revised form 27 July 2026; Accepted 13 August 2026
Available online 14 August 2026
2352-1791/© 2026 The Author(s). Published by Elsevier Ltd. This is an open access article under the CC BY-NC-ND license (http://creativecommons.org/licenses/by-nc-nd/4.0/).

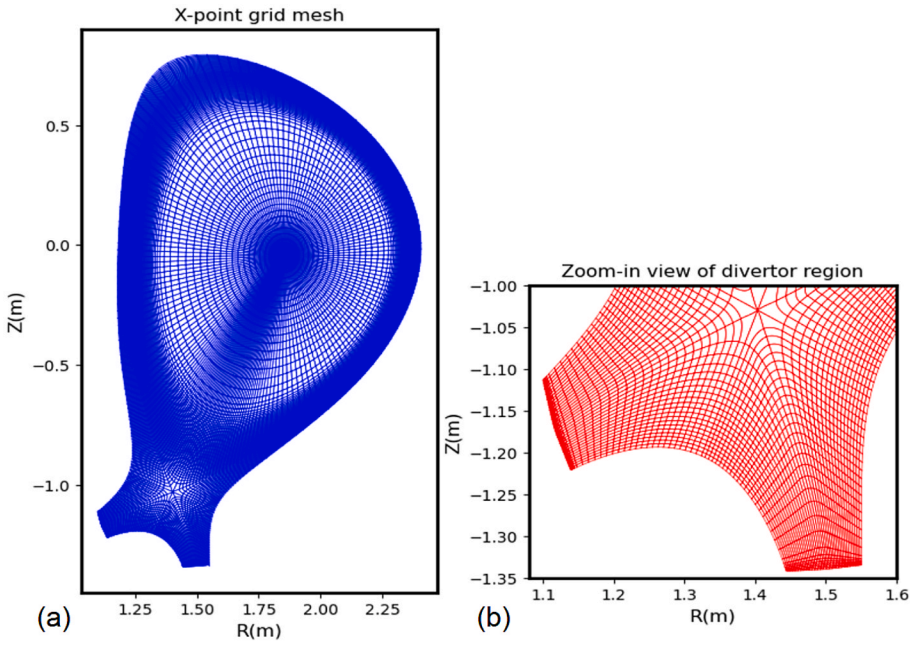

Fig. 1. Computational mesh used for the HL-3 JOREK simulations. (a) Poloidal computational domain including the core plasma, scrape-off layer (SOL), and divertor region. (b) Zoomed-in view of the divertor region, showing the refined mesh near the X-point and divertor targets.

conditions, followed by an investigation of carbon impurity transport. Furthermore, the evolution of carbon sputtering during an ELM burst is studied. Physical sputtering and chemical sputtering exhibit different transient behaviors during an ELM burst, highlighting the importance of including both mechanisms in simulations of carbon impurity production and transport.

The remainder of this paper is organized as follows: Section 2 introduces the JOREK kinetic-fluid coupled framework and the updated sputtering model. Section 3 reports the simulation setups. Section 4 presents the simulation results for carbon sputtering and impurity transport in non-ELM conditions and discusses the evolution of sputtering yields during an ELM burst. Finally, a summary is presented in Section 5.

2. Models

2.1. JOREK kinetic-fluid coupled framework

JOREK is a three-dimensional MHD code for the simulation of magnetically confined plasmas in realistic geometries. It has been extensively applied to the study of plasma behavior in both tokamaks [18] and stellarators [22,23]. Depending on the issue of interest, JOREK can solve either reduced or full MHD system, while incorporating non-ideal effects such as resistivity and viscosity. More detailed descriptions of the JOREK code and its applications can be found in the review paper [16].

The kinetic-fluid coupled framework has been developed to address physical problems involving non-fluid particles, such as neutrals, impurities, runaway electrons, and energetic particles. In this framework, the background plasma evolution is governed by the MHD equations, while the non-fluid particles are simulated using a Monte Carlo (MC) particle method. The time-dependent electromagnetic fields and local plasma parameters obtained from the fluid simulation are used to evolve MC particles self-consistently. The resulting particle information is fed back into the MHD equations, enabling a two-way coupling between the kinetic and fluid descriptions. In addition, sputtered impurity sources can be introduced dynamically according to the local plasma conditions at the plasma facing surfaces. This hybrid framework provides a practical approach for investigating impurity production and transport under evolving plasma conditions.

2.2. Kinetic-fluid coupled sputtering model

In the present model, the total sputtered carbon source is assumed to consist of physical sputtering, chemical sputtering, and self-sputtering. The corresponding sputtered carbon flux can be written as

$$\Gamma_C^{sput} = \Gamma_C^{phys} + \Gamma_C^{chem} + \Gamma_C^{self}$$

where each contribution is determined from the incident particle flux and the corresponding sputtering yield.

For physical and self-sputtering, the yield is evaluated with Eckstein's fitting formula [24], which describes the dependence of the yield on the incident particle energy (E_{in}) and angle (θ). For the physical sputtering yield, E_{in} denotes the energy of deuterium ions impinging on the target and is determined from the local plasma temperature with the sheath effect taken into account. For the self-sputtering yield, E_{in} is taken as the energy of returning carbon ions impinging on the target. The initial energy of carbon particles produced by physical sputtering and self-sputtering is assumed to follow a Thompson energy distribution depending on E_{in}.

The chemical sputtering yield is evaluated according to Roth's formula [25] with the dependence on ion flux taken into account. A fixed target-surface temperature of 500 K is imposed in both the chemical-sputtering yield model and the thermal initialization of chemically sputtered carbon particles; the wall temperature is not evolved dynamically in the present calculation.

Each sputtered carbon particle is then followed in six-dimensional phase space with a full-orbit scheme. The Lorentz equation is advanced in cylindrical geometry using the second-order Boris particle mover implemented in JOREK [21,27]. The electric and magnetic fields are interpolated from the evolving MHD solution, and the particle advance is subcycled relative to the MHD time step. Charge-state evolution is evaluated probabilistically from the local electron density and temperature using the OpenADAS SCD effective ionization and ACD effective recombination coefficients. Radiative losses include line radiation, bremsstrahlung, and recombination-related contributions, while Coulomb interactions with the background plasma are represented by a

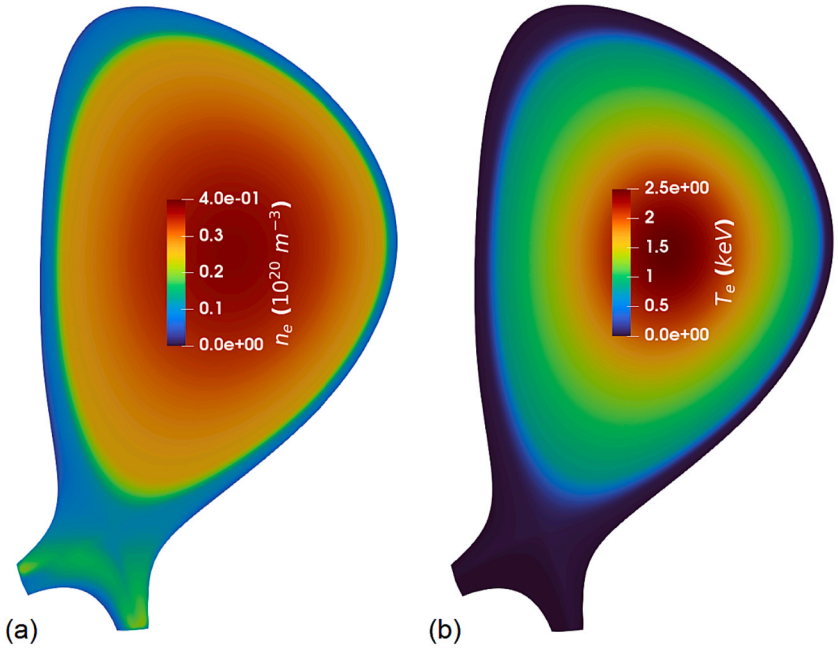

Fig. 2. Initial equilibrium profiles used in the simulations: (a) electron density and (b) electron temperature. The equilibrium is constructed from HL-3 discharge 12845.

binary-collision operator. The binary-collision operator samples a distorted-Maxwellian background distribution [20].

3. Simulation setups

This work uses the JOREK kinetic-fluid coupled framework. The background plasma is evolved with the resistive-viscous reduced-MHD model, which employs a single bulk-fluid momentum equation and a single-temperature closure, $T_i = T_e$. Among the two-fluid contributions, the ion-diamagnetic term is retained in the present setup. The sputtering process and the produced carbon impurities are treated kinetically as described in Section 2.2. The single-temperature approximation is revisited in the limitations discussion because ion and electron temperatures can differ in the scrape-off layer.

Fig. 1 shows the computational mesh used in this work. The simulated domain covers the core plasma, the scrape-off layer (SOL), and the divertor region. The computational grid is composed of 90 × 181 Bézier elements, with increased mesh density in the vicinity of the separatrix, the X-point, and the divertor targets in order to better resolve the pedestal dynamics and plasma-wall interaction processes. The plasma equilibrium is constructed based on HL-3 discharge shot 12,845 [26], with a central electron density $n_e = 3.65 \times 10^{19}$ m^{-3} and a central electron temperature $T_e = 2.5$ keV. The initial density and temperature profiles are presented in Fig. 2.

Cross-field particle and heat transport are prescribed through flux-surface-dependent double-tanh profiles in normalized poloidal flux. In the pedestal region, the particle diffusivity and perpendicular thermal diffusivity are approximately 0.39 m^2 s^{-1} and 0.31 m^2 s^{-1}, respectively. These prescribed profiles were selected to maintain near-stationary edge profiles close to the experimentally reconstructed initial state. The principal aim of the present work is to implement and assess the upgraded coupled sputtering-transport capability. The resulting target profiles are therefore presented as model results rather than direct experimental fits. Quantitative fitting to coordinated, shot-specific HL-3 edge and divertor measurements will be pursued in future work.

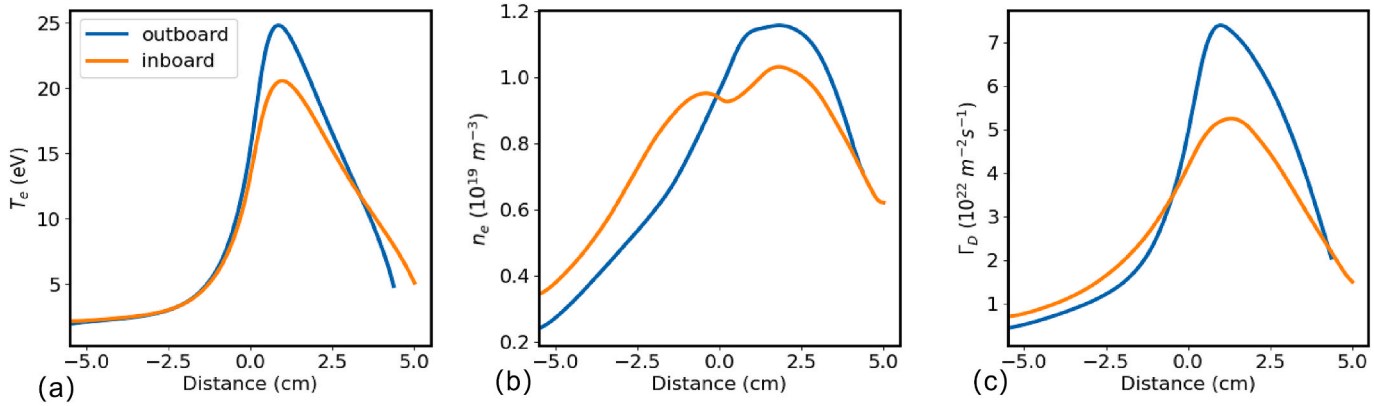

Fig. 3. Initial target plasma conditions at t = 0 ms as functions of the distance from the separatrix on the divertor target: (a) electron temperature, (b) electron density, and (c) deuterium ion flux density.

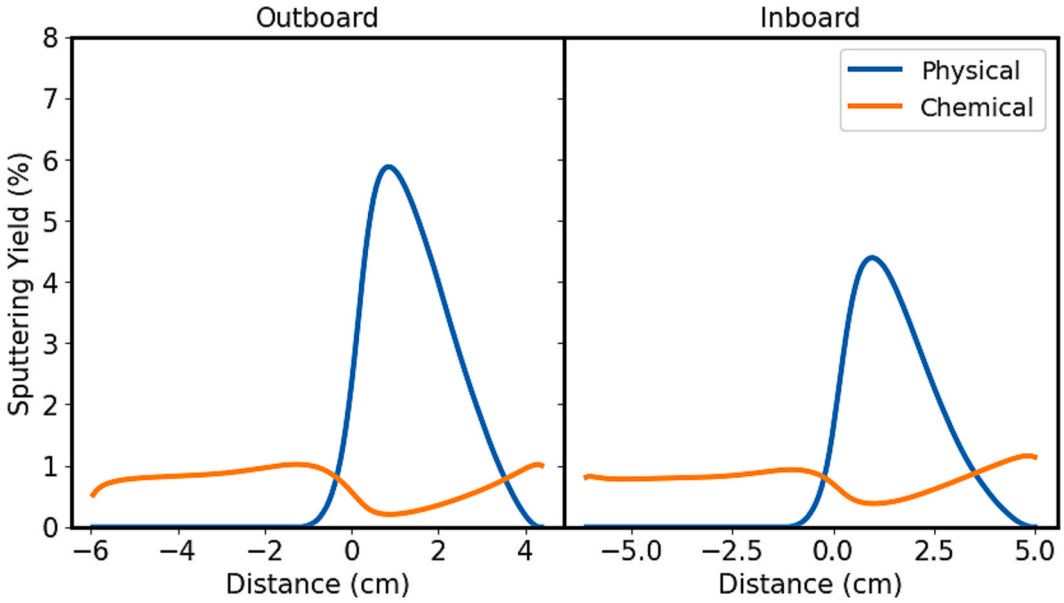

Fig. 4. Physical and chemical sputtering yields at t = 0 ms on the outboard and inboard divertor targets.

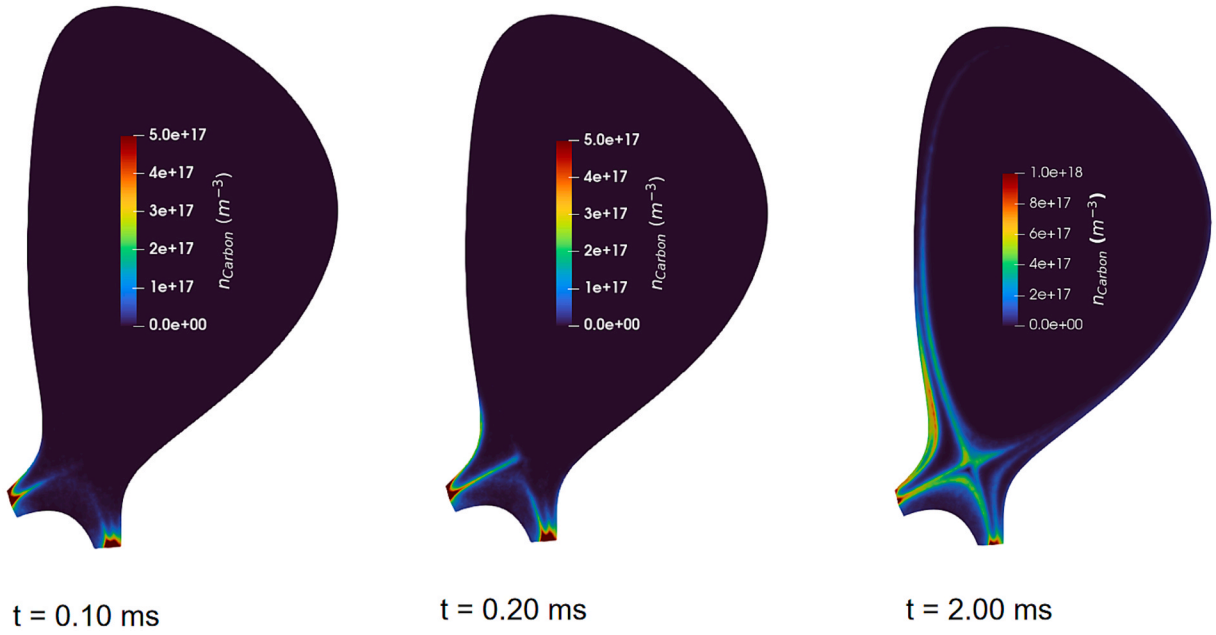

Fig. 5. Time evolution of the poloidal carbon impurity density distribution in the non-ELM simulation at t = 0.10 ms, 0.20 ms, and 2.00 ms, illustrating the transport of sputtered carbon from the divertor targets into the divertor region and SOL.

4. Simulation results

4.1. Axisymmetric simulation results without ELM

This section presents the axisymmetric simulation results in the absence of ELMs. The simulation starts from the established plasma equilibrium shown in Fig. 2, and Fig. 3 presents the plasma profiles along the divertor targets at the initial time (t = 0 ms) as a function of distance from the separatrix on the target surface. The electron temperature profiles exhibit a single peak near the strike point and then decrease gradually away from it. The peak electron temperature is about 25 eV at the outboard target and about 20 eV at the inboard target. The electron density profiles are similar at the two targets, with peak values of about 1.15×10^{19} m^{-3} and 1.0×10^{19} m^{-3} at the outboard and inboard targets, respectively. The deuterium ion flux shows a comparable trend, with peak values of approximately 7.4×10^{22} m^{-2} s^{-1} at the outboard target and 5.2×10^{22} m^{-2} s^{-1} at the inboard target. These target plasma profiles suggest that the outboard target is characterized by more intense particle and heat fluxes, and these differences are expected to directly affect the sputtering yield of carbon impurities.

Fig. 4 shows the spatial distributions of the physical and chemical sputtering yields at t = 0 ms for the outboard and inboard targets. A clear contrast is observed between the two sputtering channels: physical sputtering is sharply peaked near the strike point, whereas chemical sputtering shows a lower and more spatially extended distribution. The strong localization of physical sputtering near the strike point is mainly attributed to the higher local plasma temperature in this region. The peak physical sputtering yield reaches about 5.9 % at the outboard

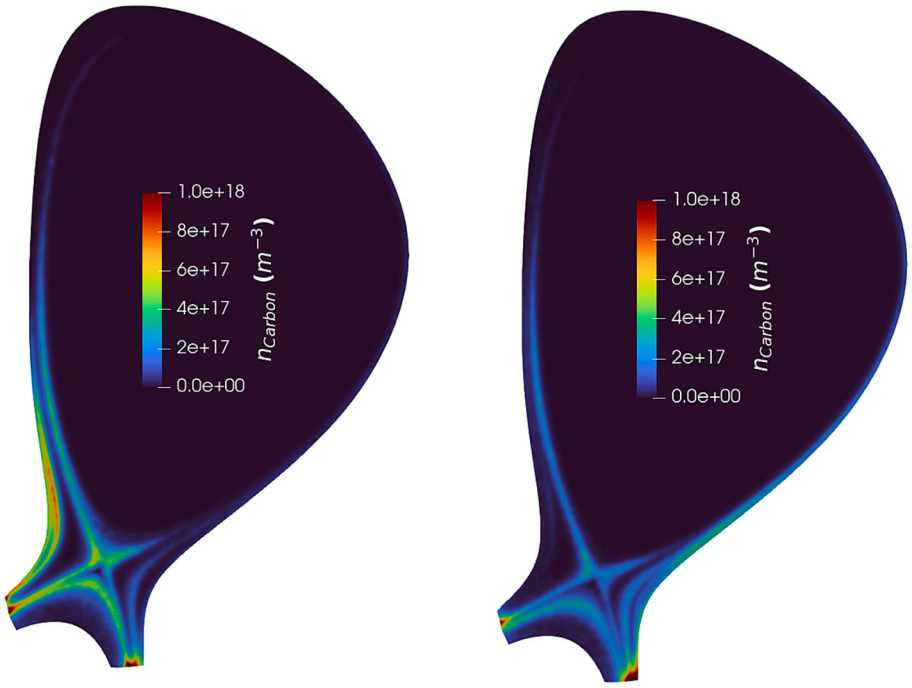

Fig. 6. (Left) The carbon impurity density at t = 2.00 ms in the normal case. (Right) The carbon impurity density at t = 2.00 ms in the case with reversed toroidal magnetic field.

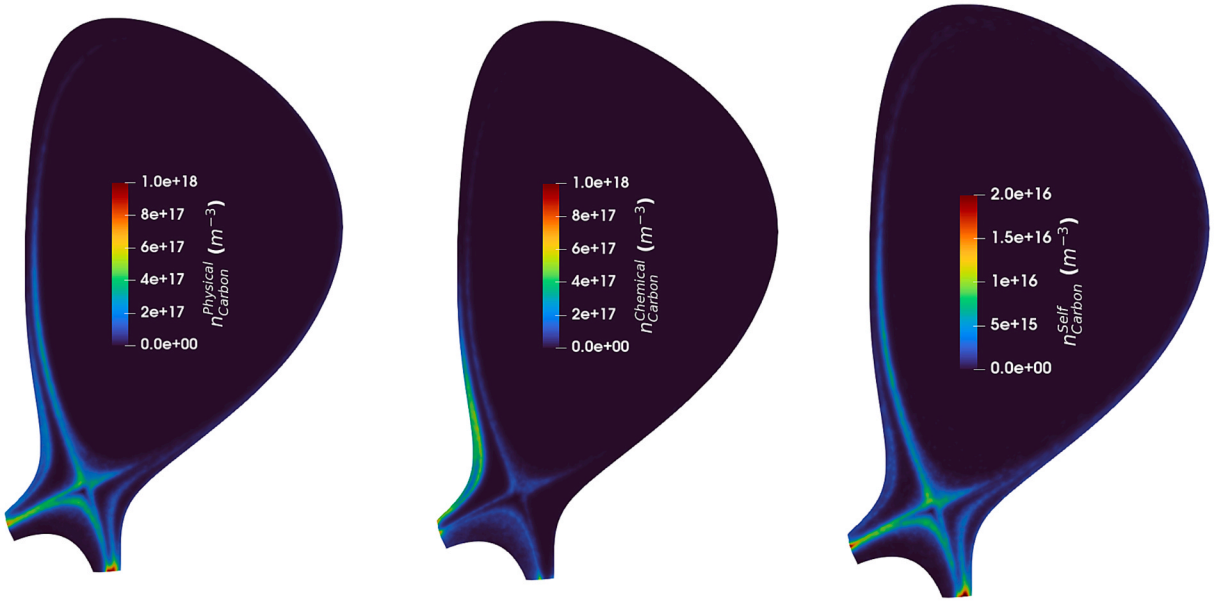

Fig. 7. Distributions of carbon impurity density associated with physical sputtering, chemical sputtering, and self-sputtering at t = 2.0 ms.

target, compared with about 4.4 % at the inboard target. By contrast, the chemical sputtering yield varies within a range from approximately 0.2 % to 1.1 % at the outboard target and from 0.4 % to 1.2 % at the inboard target. A noticeable reduction in chemical sputtering is observed near the strike point, which is mainly due to the suppression effect of the elevated ion flux.

As shown in Fig. 5, the evolution of the total carbon density reveals the transport of carbon impurities in the divertor region and the SOL. At t = 0.10 ms, carbon impurity remains strongly localized near the divertor targets. By t = 0.20 ms, the impurity distribution extends upward along the divertor legs and SOL flux tubes, forming clear field-aligned structures in the divertor region. At t = 2.0 ms, carbon impurity spreads over most of the divertor region and penetrates a significant portion of the SOL.

A pronounced asymmetry between the high-field side (HFS) and the low-field side (LFS) is observed in the carbon density distribution. This asymmetry cannot be explained solely by differences in the local sputtering source strength or the target plasma parameters. To further investigate this behavior, an additional case with reversed toroidal magnetic field was considered. Under that condition, carbon impurities accumulate more strongly on the LFS, as shown in Fig. 6, providing evidence that the observed HFS-LFS asymmetry is primarily caused by transport effects rather than by source localization.

Fig. 7 further compares the carbon density associated with different

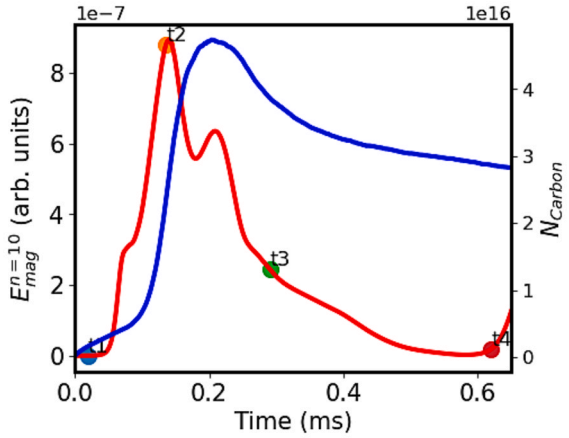

Fig. 8. Temporal evolution of the $n = 10$ perturbed magnetic energy (red curve, left axis) and the total carbon impurity content (blue curve, right axis) during the ELM simulation. The labeled times t1-t4 denote the representative pre-burst, peak-burst, decay, and relaxation phases used for the profile comparisons. (For interpretation of the references to colour in this figure legend, the reader is referred to the web version of this article.)

sputtering channels at t = 2.0 ms. The physical and chemical sputtering components exhibit similar overall spatial structures, both being mainly distributed in the divertor region and along the SOL flux tubes. Nevertheless, the chemical sputtering component shows a more pronounced extension into the HFS SOL, whereas the physical sputtering component remains more localized near the divertor target region. The self-sputtering component is much weaker, with a peak density more than one order of magnitude lower than those of the physical and chemical sputtering components. Therefore, under the present conditions, the total carbon density is dominated by the physical and chemical sputtering channels, while self-sputtering provides only a minor contribution.

4.2. Simulation results under ELM conditions

To model the plasma evolution under ELM conditions, a perturbation with toroidal mode number $n = 10$ is introduced. The $n = 10$ harmonic was selected as a representative intermediate-n peeling–ballooning case. Retaining only this harmonic avoids multimode-coupling complexity, clarifies the interaction between the MHD instability and the sputtering response, and reduces the computational resources required for the coupled calculation. Fig. 8 shows the temporal evolution of the $n = 10$ magnetic energy together with the total carbon content under ELM conditions. According to the characteristic features of the magnetic perturbation, four representative moments are denoted as t_1–t_4. Here, t_1 corresponds to the pre-ELM phase with very low perturbation amplitude, t_2 marks the strongest peak of the magnetic energy, t_3 is located in the decay stage, and t_4 represents the later relaxation phase after the burst. During this burst phase, the total carbon content increases rapidly, with a much higher growth rate than in the pre-ELM and post-ELM stages, indicating that the burst event strongly enhances carbon sputtering.

Fig. 9 shows the evolution of the pedestal electron temperature and density, as well as the corresponding divertor target electron temperature and deuterium ion flux, with the outboard target taken as an example. At t_1, clear pedestal structures are present in both T_e and n_e profiles. At the onset of the ELM, the pedestal is substantially degraded:

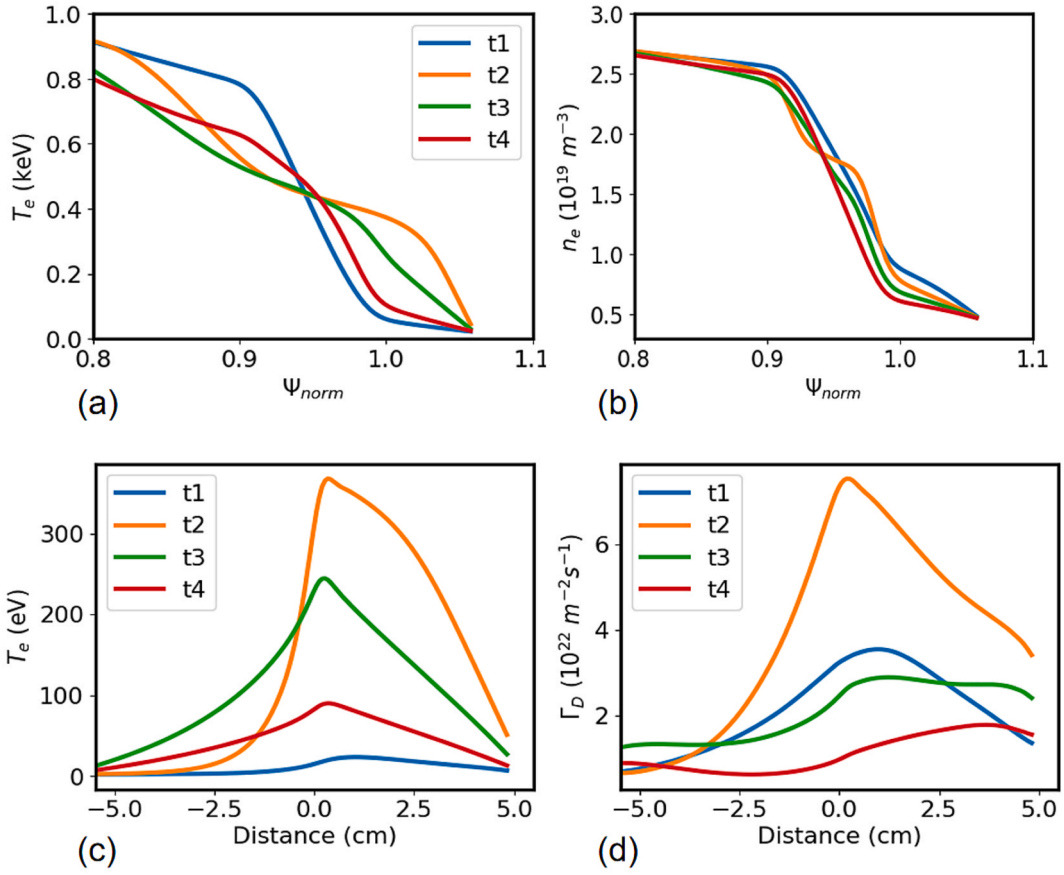

Fig. 9. The edge profiles of (a) electron temperature and (b) electron density and the distributions of (c) electron temperature and (d) deuterium ion flux density along the outboard divertor target during an ELM burst.

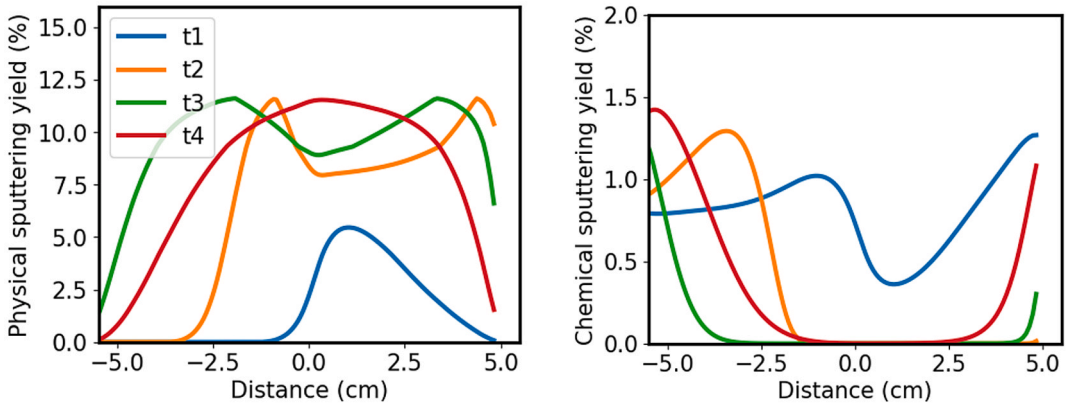

Fig. 10. Evolution of carbon sputtering yields along the outboard divertor target during the ELM burst: (a) physical sputtering yield and (b) chemical sputtering yield. The ELM enhances and broadens physical sputtering while suppressing chemical sputtering near the strike point region.

the T_e profile becomes strongly flattened, while the n_e profile also broadens with a reduced edge gradient. This reflects enhanced radial transport during the burst phase. Consistently, a response is observed at the divertor target, where both the electron temperature and deuterium ion flux rise rapidly and peak at t_2. During the decay phase t_3, the divertor target electron temperature and deuterium ion flux decrease but remain above the pre-ELM level, and they further relax at t_4.

The physical and chemical sputtering yields of carbon at the divertor target also exhibit clear temporal evolution as shown in Fig. 10. As the ELM develops, the physical sputtering yield rises sharply and broadens substantially along the target, reaching a maximum at t_2. By contrast, the chemical sputtering yield becomes strongly suppressed during the ELM burst, especially near the strike point. This indicates that the enhanced carbon release during the ELM is primarily caused by physical sputtering. The different responses of physical and chemical sputtering to the ELM burst further underline the necessity of self-consistently accounting for both mechanisms in modeling carbon impurity sputtering and transport.

5. Summary

The present results show that intrinsic carbon sputtering in HL-3 is governed by a combination of physical and chemical sputtering, and that their relative importance varies strongly with the local divertor plasma conditions. The physical sputtering is highly localized near the strike point, where the electron temperature is highest, while chemical sputtering is distributed over a broader region and becomes weaker in the strike point vicinity due to the suppression associated with the increased incident ion flux. As a result, the two channels produce distinctly different source patterns along divertor targets.

The ELM simulations further demonstrate that carbon production is highly sensitive to transient edge plasma evolution. During the burst, pedestal degradation leads to a rapid increase in divertor target temperature and deuterium ion flux, which strongly enhances physical sputtering and broadens its distribution along the target. In contrast, chemical sputtering is significantly reduced during the same phase, especially near the strike point. Therefore, a self-consistent treatment of both physical and chemical sputtering is essential for reliable modeling of carbon impurity behavior and plasma-wall interaction in HL-3.

The present study focuses on establishing and assessing the upgraded coupled sputtering-transport framework and on characterizing the simulated carbon-source response under ELM conditions. The results should be interpreted in light of two aspects that motivate further development. First, the single-temperature closure $T_i = T_e$ may underestimate ion-driven sputtering in regions where T_i exceeds T_e or has a broader radial profile, particularly in the far SOL. Second, quantitative comparison with coordinated, shot-specific HL-3 measurements remains to be performed. Developing a two-temperature background model and carrying out this quantitative comparison will therefore be important directions for future work.

CRediT authorship contribution statement

Z. Liang: Writing – original draft, Methodology, Investigation, Conceptualization. **Y.L. Liu:** Methodology. **Y. Feng:** Methodology. **S.Y. Dai:** Supervision, Conceptualization. **M. Hoelzl:** Writing – review & editing. **A. Cathey:** Writing – review & editing. **D. Hu:** Writing – review & editing. **S.Q. Korving:** Writing – review & editing. **Y.C. Liang:** Writing – review & editing. **M. Szucs:** Writing – review & editing. **Y. Zhang:** Resources. **D.Z. Wang:** Funding acquisition. **the Jorek Team:** Software.

Declaration of competing interest

The authors declare that they have no known competing financial interests or personal relationships that could have appeared to influence the work reported in this paper.

Acknowledgments

This work is supported by the National Magnetic Confinement Fusion Science Program No. 2022YFE03020001, National Natural Science Foundation of China under Grant Nos. 12235002 and 12475213, the Open Basic Research Fund under the 'Top-Talent-Led Project' System of Southwest Institute of Physics (No. 2025DWKF007). This work has been carried out within the framework of the EUROfusion Consortium, funded by the European Union via the Euratom Research and Training Programme (Grant Agreement No 101052200-EUROfusion). Views and opinions expressed are however those of the author(s) only and do not necessarily reflect those of the European Union or the European Commission. Neither the European Union nor the European Commission can be held responsible for them. The views and opinions expressed herein do not necessarily reflect those of the ITER Organization.

Data availability

Data will be made available on request.

References

[1] J.N. Brooks, et al., Erosion/redeposition analysis: status of modeling and code validation for semi-detached tokamak edge plasmas, J. Nucl. Mater. 266–269 (1999) 58–66.
[2] L. Wang, et al., Advances in plasma–wall interaction control for H-mode operation over 100 s with ITER-like tungsten divertor on EAST, Nucl. Fusion 59 (2019) 086036.

[3] K. Krieger, et al., Scrape-off layer and divertor physics: chapter 5 of the special issue: on the path to tokamak burning plasma operation, Nucl. Fusion 65 (2025) 043001.
[4] A.W. Leonard, Edge-Localized-Modes in Tokamaks, Phys. Plasmas 21 (2014) 090501.
[5] A. Loarte, et al., Characteristics of type I ELM energy and particle losses in existing devices and their extrapolation to ITER, Plasma Phys. Control. Fusion 45 (2003) 1549–1569.
[6] K. Verhaegh, et al., An improved understanding of the roles of atomic processes and power balance in divertor target ion current loss during detachment, Nucl. Fusion 59 (2019) 126038.
[7] I. Senichenkov, et al., Detached regime with highly radiating X-point: physics and modelling, Contrib. Plasma Phys. 62 (2022) e202100177.
[8] R.A. Pitts, et al., A full tungsten divertor for ITER: Physics issues and design status, J. Nucl. Mater. 438 (2013) S48–S56.
[9] G.Y. Zheng, et al., Investigations on the heat flux and impurity for the HL-2M divertor, Nucl. Fusion 56 (2016) 126013.
[10] L. Chen, et al., L–H power threshold studies with tungsten/carbon divertor on the EAST tokamak, Radiat. Eff. Defect. S. 171 (2016) 359–373.
[11] R. Mao, et al., Plasma simulation of complex HL-2M divertor geometries using SOLEDGE2D-EIRENE edge plasma transport code, Contrib. Plasma Phys. 58 (2018) 781–790.
[12] L. Xue, et al., Integrated plasma scenario analysis for the HL-2M tokamak, Nucl. Fusion 60 (2020) 016016.
[13] X.R. Duan, et al., Progress of HL-2A experiments and HL-2M program, Nucl. Fusion 62 (2022) 042020.
[14] Z. Liang, et al., First EMC3-EIRENE simulation of edge plasma behavior and heat flux deposition on divertor target on HL-2M, Fusion Eng. Des. 159 (2020) 111803.
[15] Z. Liang, et al., Estimations of edge plasma and impurity performance on HL-2M with EMC3-EIRENE modelling, Phys. Scr. 96 (2021) 065601.
[16] M. Hoelzl, et al., The JOREK non-linear extended MHD code and applications to large-scale instabilities and their control in magnetically confined fusion plasmas, Nucl. Fusion 61 (2021) 065001.
[17] M. Hoelzl, et al., Advances in 3D transient plasma dynamics and control through MHD and hybrid fluid-kinetic simulations with JOREK, Nucl. Fusion 66 (2026) 116006.
[18] G.T.A. Huijsmans, et al., Modelling of edge localised modes and edge localised mode control, Phys. Plasmas 22 (2015) 021805.
[19] S.Q. Korving, et al., Development of the neutral model in the nonlinear MHD code JOREK: Application to E × B drifts in ITER PFPO-1 plasmas, Phys. Plasmas 30 (2023) 042509.
[20] Y. Homma, et al., Kinetic modelling for neoclassical transport of high-Z impurity particles using a binary collision method, Nucl. Fusion 56 (2016) 036009.
[21] D.C. Van Vugt, et al., Kinetic modeling of ELM-induced tungsten transport in a tokamak plasma, Phys. Plasmas 26 (2019) 042508.
[22] R. Ramasamy, et al., Nonlinear MHD modeling of soft β limits in W7-AS, Nucl. Fusion 64 (2024) 086030.
[23] R. Ramasamy, et al., Nonlinear MHD simulations of external kinks in quasi-axisymmetric stellarators using an axisymmetric external rotational transform approximation, Nucl. Fusion 61 (2021) 076017.
[24] W. Eckstein, R. Preuss, New fit formulae for the sputtering yield, J. Nucl. Mater. 320 (2003) 209–213.
[25] J. Roth, et al., Flux dependence of carbon chemical erosion by deuterium ions, Nucl. Fusion 44 (2004). L21–5.
[26] Y. Zhang, et al., First experimental observation of QH-mode with EHOs on the HL-3 tokamak, Nucl. Fusion 66 (2026) 016054.
[27] G.L. Delzanno, E. Camporeale, On particle movers in cylindrical geometry for Particle-In-Cell simulations, J. Comput. Phys. 253 (2013) 259–277.